

# CO<sub>2</sub> laser based two-volume collective scattering instrument for spatially localized turbulence measurements

M. Saffman<sup>a)</sup>

*Optics and Fluid Dynamics Department, Risø National Laboratory, EURATOM Association, DK-4000 Roskilde, Denmark*

S. Zoletnik

*CAT-SCIENCE Bt. Detrekö u., 1/b H-1022 Budapest, Hungary*

N. P. Basse and W. Svendsen

*Optics and Fluid Dynamics Department, Risø National Laboratory, EURATOM Association, DK-4000 Roskilde, Denmark and Ørsted Laboratory, H.C. Ørsted Institute, Universitetsparken 5, DK-2100 Copenhagen Ø, Denmark*

G. Kocsis

*Central Research Institute for Physics—Research Institute for Particle and Nuclear Physics, P.O. Box 49, H-1525 Budapest, Hungary*

M. Endler

*Max-Planck-Institut für Plasmaphysik, EURATOM Association, D-85748 Garching, Germany*

(Received 14 September 2000; accepted for publication 10 April 2001)

We describe and demonstrate a two-volume collective scattering system for localized measurements of plasma turbulence. The finite crossfield correlation length of plasma turbulence combined with spatial variations in the magnetic field direction are used to obtain spatially localized turbulence measurements at the Wendelstein 7-AS fusion experiment. By comparing with localized measurements obtained using the single wide beam technique [Truc *et al.*, *Rev. Sci. Instrum.* **63**, 3716 (1992)] we provide a proof-of-principle demonstration of the two-beam method. An optimized configuration with large toroidal separation of the measurement volumes is predicted to be capable of providing spatial resolution better than 5 cm. © 2001 American Institute of Physics. [DOI: 10.1063/1.1376655]

## I. INTRODUCTION

Fluctuation measurements are essential in order to continue progress towards an understanding of the role of turbulence in transport of energy within magnetically confined plasmas. Although there is an accumulated body of evidence showing a connection between plasma turbulence and transport between the core and edge regions of the plasma a precise understanding of the operation and optimization of toroidal magnetic fusion devices remains a challenge.<sup>1–4</sup> It is now apparent that spatially localized fluctuation measurements, at an arbitrary position in the plasma volume, will be needed in order to achieve a detailed understanding of the mechanisms by which turbulence affects confinement. In this article we report on the design and application of a two-volume collective scattering instrument for obtaining turbulence measurements with enhanced spatial localization.

Collective scattering of 10.6 μm CO<sub>2</sub> laser radiation is a well-established and widely used technique for measurements of waves and turbulence in plasmas.<sup>5–11</sup> Since the frequency of 10.6 μm radiation is much greater than the plasma frequency in fusion machines, absorption and refraction of the beam are negligible which makes the CO<sub>2</sub> laser a valu-

able tool for probing the entire plasma volume. Traditional collective scattering using the CO<sub>2</sub> laser provides measurements of wave numbers in a range of order 1–100 cm<sup>-1</sup>. This range covers both microturbulence at the highest wave numbers as well as the large scale coherent structures at small wave numbers that are believed to play a significant role in transport processes. The main drawback of CO<sub>2</sub> laser based collective scattering measurements is that they do not give good spatial resolution on small to medium sized fusion plasma experiments.

The limited spatial resolution of collective scattering can be explained by the following scaling arguments. Laser light with wavelength λ and wave number  $k = 2\pi/\lambda$  scatters from electron density fluctuations with wave number κ. The scattered light propagates at an angle  $\theta = \kappa/k$  with respect to the incident laser beam. If the laser beam is focused in the plasma to a diameter  $d_{\text{beam}}$  then the characteristic length of the region from which light is scattered is of order  $L = 2d_{\text{beam}}/\theta = 2d_{\text{beam}}k/\kappa$ . In order to limit the scattering volume length  $L$  we must reduce  $d_{\text{beam}}k$  or increase κ. To obtain resolution in wave number and to be able to separate the scattered light from the directly transmitted light we need  $d_{\text{beam}}$  several times larger (say  $N$  times) than the fluctuation wavelength  $\Lambda = 2\pi/\kappa$ . Furthermore, in order for the scattering to be collective we must have a Salpeter parameter  $\alpha_S = k_D/(2\pi\kappa) > \alpha_{S,\text{min}}$ , where  $k_D$  is the Debye wave number

<sup>a)</sup>Present address: Dept. of Physics, University of Wisconsin, Madison, WI 53706; electronic mail: msaffman@facstaff.wisc.edu

in the plasma. Thus, the scattering volume length is bounded below by  $L > 2N(2\pi)^3 k \alpha_{S,\min}^2 / k_D^2$ . Assuming a typical Debye length of  $5 \times 10^{-5}$  m, a laser wavelength of  $10.6 \mu\text{m}$ ,  $N=3$ , and  $\alpha_{S,\min}=2$  gives  $L > 22$  cm. We see that even working with  $\alpha_S=2$ , which must be considered as a lower limit for collective scattering (for the stated parameters  $\alpha_S=2$  corresponds to  $\kappa=100 \text{ cm}^{-1}$ ), the axial resolution is at best of order a quarter meter which is comparable with the plasma diameter on small to medium sized fusion experiments.

Modifications of the basic collective scattering technique have been proposed and demonstrated with the aim of improving the spatial resolution of the measurements. These methods can be grouped into two categories: those that rely on a modification of the optical system and those that rely on spatial variations of a physical parameter in the plasma other than the density. Variations to the basic collective scattering arrangement have included correlations between multiple scattering directions,<sup>12</sup> and tomographic inversion of the data from multiple beams.<sup>13</sup> In the second category variations in the radial electric field,<sup>14</sup> or changes in the direction of the magnetic field lines with spatial position, combined with the fact that the turbulent fluctuations are primarily confined to a plane perpendicular to the local magnetic field,<sup>15</sup> have been used for obtaining localized measurements.

In the present article we describe and demonstrate a new approach to spatially localized measurements that combines correlations between two separated measurement volumes, with spatial rotation of the magnetic field lines. Plasma turbulence has a finite cross field correlation length. Measurements in the scrape-off layer of both the Axially Symmetric Divertor Experiment tokamak and the Wendelstein 7-AS stellarator indicated correlation lengths of the order of 1 cm.<sup>16</sup> Similar lengths were observed in the core plasma of the Tokamak Fusion Test Reactor tokamak.<sup>17</sup> Therefore a strong correlation between measurements from two spatially separated volumes will only be registered if the volumes are connected by a magnetic field line. As we show below by varying the measurement volume separation toroidally and radially and taking advantage of the magnetic field pitch angle variation we obtain a diagnostic which combines the correlation technique of Ref. 12 and the magnetic localization technique of Ref. 15.

The intrinsic resolution that can be achieved with two narrow beams, or a single wide beam with a diameter equal to the separation of the narrow beams, is about the same. However, in a single beam experiment spatial resolution is achieved by using a wide scattering beam with a good wave number resolution. The beam width cannot be increased arbitrarily due to both practical limits and to the fact that a beam of width  $w$  inherently integrates over a radial region of size  $w$ . Using two narrow beams these limitations can be relaxed and the spatial resolution can be further enhanced. Furthermore, because the two-beam technique described here relies on correlation measurements, whereas the wide beam technique<sup>15</sup> uses the signal from a single scattering volume, there are important differences in the operation of the two methods. The wide beam technique relies on the plasma fluctuations being locally perpendicular to the magnetic field

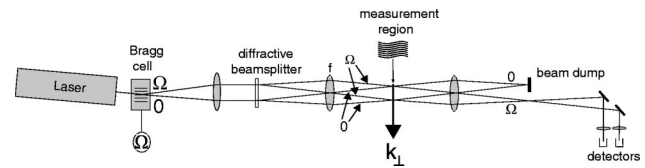


FIG. 1. Optical system for creating two parallel measurement volumes. The Bragg cell gives a frequency shift  $\Omega$  to the diffracted beam.

lines, while localization with two separated beams relies on the assumption of fluctuation transport along the field lines. As we discuss in more detail below this allows us to propose an optimized two-beam configuration with large toroidal separation that uses the magnetic field geometry to obtain very high spatial resolution.

The rest of the article is organized as follows. The measuring system is described in Sec. II. We pay particular attention to the digital data acquisition system which enables time resolved spectra and correlations to be acquired over the entire length of a 1 s plasma discharge. Data processing algorithms for reliable estimation of correlation functions in the time and frequency domains at low signal to noise ratio are described. Installation of the system at W7-AS and results from line integrated turbulence measurements are given in Sec. III. Spatially localized measurements using both the single and dual beam techniques are described in Sec. IV. We summarize our results and provide an outlook for future measurements in Sec. V.

## II. DESCRIPTION OF THE MEASUREMENT SYSTEM

### A. Optical system

The optical approach used to generate two measurement volumes is shown in Fig. 1. A portion of the laser output is deflected into a local oscillator (LO) beam by a Bragg cell and then made to propagate in parallel with the main beam using a lens. The two beams are then each split with a diffractive optical element and Fourier transformed with lens  $f$ . In the back focal plane of the lens we get two pairs of crossing regions, where pairs of frequency shifted beams interfere. Fourier transforming again after the measurement region spatially separates the main beams from the frequency shifted beams. The main beams are then blocked and the remaining beams focused onto two detectors.

The measurement volumes are separated by  $d_{MV} = \theta_{BS} f$ , where  $\theta_{BS}$  is the full angle between the beams diffracted by the beam splitter, and  $f$  is the focal length of the transforming lens. The angle between the interfering beams is given by  $\theta_{MV} = d_{BS} / f$ , where  $d_{BS}$  is the separation of the parallel beams at the beam splitter. The optical system described below has, for a given choice of lenses, fixed  $\theta_{BS}$  and hence fixed measurement volume separation, while  $d_{BS}$  is continuously variable so that different fluctuation wave numbers can be selected.

The measurement volume region where the main and LO beams cross contains a set of parallel interference fringes with spacing  $\Lambda = \lambda / \theta_{MV}$ . The number of fringes in the measurement volume can be defined as  $N = d_{beam} / \Lambda = 2w / \Lambda$ , where  $w$  is the Gaussian radius of the laser beams. Provided

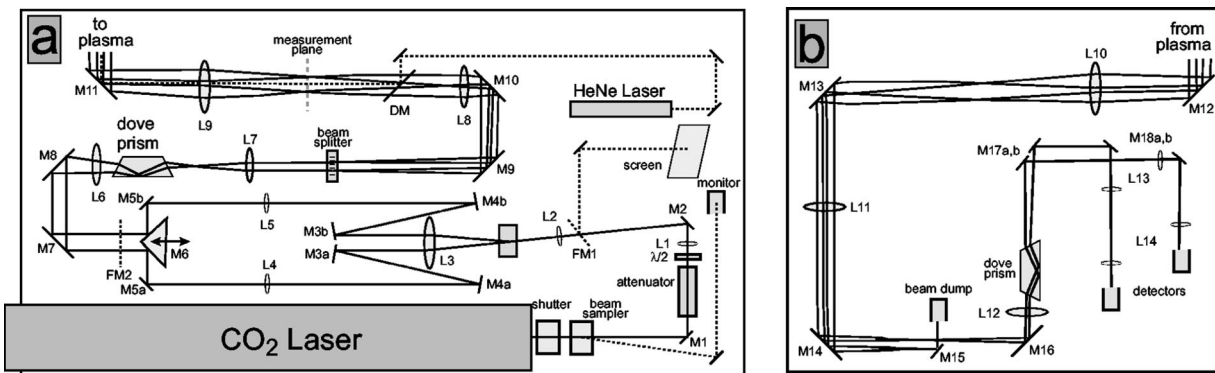


FIG. 2. Optical layout: (a) Transmitting optics table and (b) receiving optics table. The components are M1—18 mirrors, L1—14 lenses, FM1—two movable mirrors, DM dichroic mirror.

that  $N$  is somewhat larger than unity heterodyne detection of the scattered light results in a signal proportional to the magnitude of the density fluctuations at wavenumber  $\kappa = |\mathbf{k}_\perp| = 2\pi/\Lambda$ . The wave number resolution is given by  $\Delta\kappa = 2/w$ .

The actual implementation of this scheme is shown in Fig. 2. The transmitter table is located underneath and some meters away from the W7-AS vacuum vessel. The light source is a 20 W continuous wave CO<sub>2</sub> laser with a diffraction grating serving as the mirror at the back of the cavity for selection of a single oscillation line. Fine adjustment of the position of the output coupler using a piezoelectric transducer is used to obtain near Gaussian single transverse mode operation, and to minimize beatnotes between higher order transverse modes and the main TEM<sub>00</sub> output. The position of the output coupler is actively stabilized using a feedback system. The output coupler is dithered at 700 Hz, and an error signal is derived by synchronously detecting the resulting modulation of the intracavity intensity, as monitored with a photodiode that collects the weak light reflected from one of the laser tube Brewster windows.

A small portion of the laser output beam is split off with a diffractive beam sampler in order to monitor the laser stability and presence of transverse mode beats. Movable mirror FM1 can be inserted into the beam path to view the spatial structure on an infrared sensitive screen. The laser beam is passed through a variable attenuator and half-wave plate before being focused into an acoustic wave Ge Bragg cell which angularly deflects and frequency shifts a portion of the main beam by 40 MHz. The power of the resulting LO beam is continuously variable by adjusting the radio frequency power driving the Bragg cell. The main transmitted beam and the LO beam are relayed to a 90° prism (M6) that is used to adjust the separation between the beams. The parallel beams are then sent through a ZnSe dove prism that rotates the plane containing the beams. The dove prism is used to align the direction of the measured  $\mathbf{k}_\perp$  relative to the plasma. After the dove prism the beams are sent through a ZnSe diffractive beam splitter that splits each beam into two, with an angle of 25 mrad between the beams. Fourier transforming the beams gives two measurement volumes where a main and LO beam cross, located in the front focal plane of lens L9. Higher order beams from the diffractive beam splitter are blocked with an aperture in this plane. Rotating the diffrac-

tive beam splitter rotates the position of the measurement volumes on a circle, while leaving the magnitude and direction of  $\mathbf{k}_\perp$  unchanged. The rest of the optical train, including three relay lenses not shown in the figure, serves to relay the measurement volume in front of L9 to the desired position in the plasma. A HeNe laser beam is introduced into the optical path after the diffractive beam splitter as an aid to alignment. All lenses are antireflection coated ZnSe.

The four laser beams are focused into the plasma with a  $f = 1.38$  m transmitting lens, collected on the other side with a  $f = 1.08$  m receiving lens, and relayed onto the receiving table mounted above the W7-AS vacuum vessel. The receiving table optics shown in Fig. 2(b) serve to separate the main and LO beams, and to correct for beam rotations introduced by the dove prism and the diffractive beam splitter on the transmitting optics table. At a plane corresponding to an image plane of the diffractive beam splitter mirror M15 is used to deflect the main beams into a beam dump. The laser power can also be monitored at this point with a thermal detector. The LO beams, which after passing through the plasma contain the local oscillators plus the light scattered out of the main beams due to plasma fluctuations, are then sent through a second dove prism that can be rotated in unison with the diffractive beam splitter. In this way changes in the measurement volume positions are compensated so that the detectors can be fixed on the receiving table. The closely spaced beams are separated at mirrors M17a and M17b and sent to two identical detectors.

## B. Signal detection and acquisition

The scattered light and local oscillator beams are focused onto photoconductive HgCdTe detectors.<sup>18</sup> The detectors operate at room temperature and have an active area of 1 mm<sup>2</sup>. The detectors are biased with a constant current, as shown in Fig. 3 and the output signals are amplified and buffered with line drivers before being recorded with a custom electronic card installed in a computer located by the laser and transmitting optics.

The detector signals are centered at the Bragg cell frequency of 40 MHz and may be modulated by waves in the plasma in a band of up to  $\pm 10$  MHz about the carrier frequency. Direct digital acquisition of these signals throughout plasma discharges lasting up to 1 s was deemed impractical.

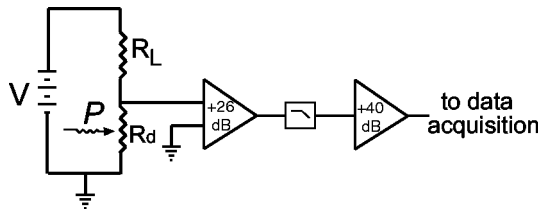


FIG. 3. Detector electronics. The combined noise effective impedance of the detector, the load resistor, and the preamplifier is  $R_{\text{eff}} = R_{\text{eq}} R_{\text{eff,pa}} / (R_{\text{eq}} + R_{\text{eff,pa}})$ , where  $R_{\text{eq}} = R_d R_L / (R_d + R_L)$  is the equivalent parallel resistance of the detector resistance  $R_d$  and load resistance  $R_L$ , and  $R_{\text{eff,pa}} = R_{\text{pa}} 10^{-\text{NF}/10}$ , where NF is the preamplifier noise figure in dB and  $R_{\text{pa}}$  is the preamplifier input resistance. Circuit parameters:  $R_d \approx 50 \Omega$ ,  $R_L = 950 \Omega$ ,  $R_{\text{pa}} = 50 \Omega$ ,  $\text{NF} = 2.8 \text{ dB}$ .

We chose, therefore, to reduce the data rate by recording and demodulating the signals. The signals are processed by a specially designed two-channel quadrature demultiplexer on a PCI bus card, as shown schematically in Fig. 4. Either analog or digital demodulation of the signals is possible. A design study of both approaches favored the lower cross talk between upper and lower sidebands, increased flexibility in signal filtering, and more predictable performance achievable with a digital design. The demultiplexer is a dual channel digital data-acquisition card with a fast 8 bit analog/digital converter sampling at 160 Msamples/s per channel. Sampling is done phase locked with the 40 MHz driving frequency of the Bragg cell, that is 4 times in one period. The four samples are mixed down to baseband by multiplying with  $\exp(-i\pi n/2)$ ,  $n=0, 1, 2, 3$  which gives  $[1, -i, -1, i]$  corresponding to sequences of  $[1, 0, -1, 0]$  and  $[0, -1, 0, 1]$  for the two quadrature channels. Note that every second sample is zero, and can be thrown away without loss of information. The signals are then digitally low-pass filtered. The data rate is reduced (decimated) by a factor of 4 or 6 supplying up to 80 Mbytes of data per second. The data is transferred to the main memory of the host personal computer (Intel  $\times 86$  architecture) by direct memory access transfer.

The two signals per channel resulting from the digital processing constitute the real and imaginary parts of the scattering signals. The effective sampling rate of these complex signals is 20 or 16 MHz for decimation by 4 and 6, respectively. Due to the method of digital processing the real and imaginary parts of the complex signal are shifted in time by  $1/160 \mu\text{s}$ . This is corrected during the off-line data evaluation as explained in Sec. IID.

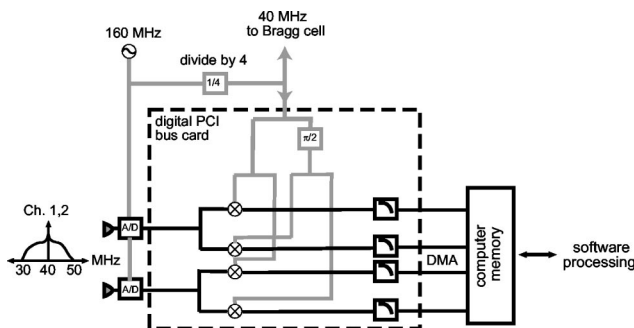


FIG. 4. Schematic of electronic signal acquisition and processing layout.

**C. Signal to noise ratio**

In order to evaluate the feasibility of a plasma turbulence measurement it is necessary to estimate the expected signal to noise ratio of the detected signals. To calculate the optical power scattered from the plasma we can assume that the electron density  $n_e$  is spatially modulated in the form  $n_e(x) = n_{e0} [1 + \delta n_e \cos(\kappa x)]$ . The standard expression for the scattered power is then<sup>19</sup>

$$P = P_{\text{inc}} \pi \frac{L^2}{k^2} (\pi r_e^2) (n_{e0} \delta n_e)^2, \tag{1}$$

where  $P_{\text{inc}}$  is the incident power and  $r_e$  is the classical electron radius. Note that the scattered power is independent of the diameter of the incident beam assuming a uniform plasma.

Equation (1) provides an upper limit on the scattered power, but is not immediately usable for estimating the signal to noise ratio since it includes contributions from the entire range of fluctuation wave numbers present in the plasma. Only a small fraction of the entire turbulence spectrum is actually detected due to the filtering property of the Gaussian laser beams. To account for this note that the density fluctuations can be written as  $\delta n_e^2 = \int_{k_{\text{min}}}^{\infty} dk \delta n_e^2(k)$ . The turbulence spectrum typically has a power law decay,  $\delta n_e^2(k) = a/k^m$ , where  $m$  is the decay exponent and  $a$  is a constant. An exponent of  $m=3$  is typical for plasma turbulence and a similar value is also found at W7-AS, see Sec. III below. Using  $m=3$  gives  $\delta n_e^2(k) = 2k_{\text{min}}^2 \delta n_e^2/k^3$ . We therefore replace Eq. (1) by

$$P = P_{\text{inc}} \pi \frac{L^2}{k^2} (\pi r_e^2) n_{e0}^2 \int_{k_{\text{min}}}^{\infty} dk \delta n_e^2(k) f(k), \tag{2}$$

where  $f(k)$  is an instrumental filter function that describes the sensitivity to different fluctuation wave numbers. For a Gaussian laser beam  $f(k)$  is a Gaussian in  $k$  with width  $2/w$ , where  $w$  is the radius of the beam in the plasma.  $f(k)$  is centered at  $k_{\text{meas}}$ , where  $k_{\text{meas}}$  is the central measured wave number selected by the optical setup. Equation (2) can be evaluated exactly in terms of error functions. For our purposes it is sufficient to assume that  $f(k)$  is unity for  $k_{\text{meas}} - 1/w < k < k_{\text{meas}} + 1/w$ , and zero elsewhere. Approximating the integral over  $k$  by  $\delta n_e^2(k_{\text{meas}}) 2/w$  we obtain

$$P = P_{\text{inc}} \pi \frac{L^2}{k^2} (\pi r_e^2) (n_{e0} \delta n_e)^2 \frac{4k_{\text{min}}^2}{w k_{\text{meas}}^3}. \tag{3}$$

Measurements of plasma turbulence indicate that  $k_{\text{min}} = 1 \text{ cm}^{-1}$  is a reasonable estimate for the wave number where the turbulence is maximum. Parameters corresponding to typical discharge conditions at W7-AS are  $n_{e0} \sim 10^{19} \text{ m}^{-3}$  and  $\delta n_e \sim 10^{-2}$ . As we discuss below fluctuation levels depend strongly on the position in the plasma. Recent measurements of cm scale turbulence at W7-AS<sup>20</sup> indicate that while  $\delta n_e \sim 10^{-2}$  is typical in the core of the plasma, the relative fluctuation level increases by an order of magnitude near the plasma edge.

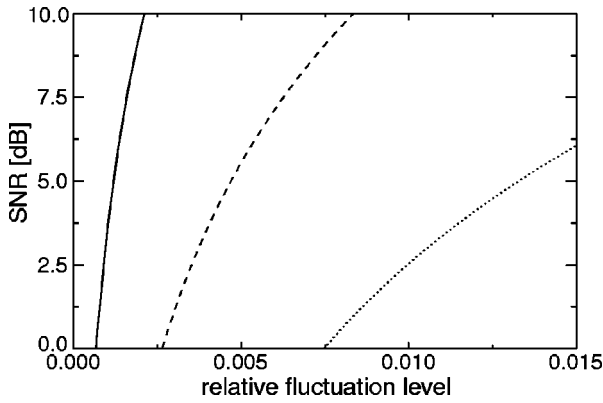


FIG. 5. Estimated signal to noise ratio as a function of relative fluctuation level for  $k_{\text{meas}}=10$  (solid line), 25 (dashed line), and  $50 \text{ cm}^{-1}$  (dotted line) and  $w=3 \text{ mm}$ .

With room temperature detectors the dominant noise source is thermal fluctuations of the current. In this limit the signal to noise ratio of the heterodyne signal is<sup>21</sup>

$$\text{SNR} = \frac{R_{\text{eff}}}{4k_B T B} \left( \frac{\eta \eta_{\text{hd}} e G}{h \nu} \right)^2 \mathcal{P} \mathcal{P}_{\text{lo}}, \quad (4)$$

where  $\mathcal{P}_{\text{lo}}$  is the local oscillator power,  $G$  is the photoconductive gain,  $e$  is the electron charge,  $\eta$  is the detector quantum efficiency,  $\eta_{\text{hd}}$  is the heterodyning efficiency,  $\nu$  is the optical frequency,  $h$  is Planck’s constant,  $k_B$  is the Boltzmann constant,  $T$  is the temperature, and  $B$  is the detection bandwidth. Figure 5 shows the signal to noise ratio calculated using Eqs. (3) and (4) for three different values of  $k_{\text{meas}}$  with the plasma parameters listed above and  $\mathcal{P}_{\text{inc}}=10 \text{ W}$ ,  $\mathcal{P}_{\text{lo}}=0.5 \text{ W}$ ,  $\eta=0.5$ ,  $\eta_{\text{hd}}=0.9$ ,  $G=5. \times 10^{-3}$ ,<sup>22</sup> and  $B=10 \text{ MHz}$ . The calculations show that for the expected fluctuation levels measurements with unity signal to noise ratio are possible at wavenumbers not greatly exceeding  $50 \text{ cm}^{-1}$ . This is consistent with the data for W7-AS we present in the following sections which describe measurements with a maximum wave number of  $61 \text{ cm}^{-1}$ .

**D. Signal processing**

As described in Sec. II B the electronic system provides complex signals for both channels with various effective sample rates defined by the decimation filter. These complex signals are analyzed off line with programs written in Interactive Data Language. The data are first corrected for a fixed time shift between the quadrature components. After time shift correction the data are used for calculating and plotting raw signals, power spectra, probability distributions, correlations, and various other quantities calculated from these.

The first task of the data analysis programs is to correct for the  $1/160 \mu\text{s}$  time delay between the real and imaginary parts of the signals caused by the implementation of the digital quadrature detection. This correction can be done either in the time or frequency domains. A perfect correction can be done in the frequency domain in the following way. In the measured complex signal  $S(t)$  the imaginary and real parts are measured at different times with time difference  $\delta t$ :

$$S(t) = a(t) + ib(t - \delta t). \quad (5)$$

By calculating the Fourier transform of the corrupted signal one can see that the time delay mixes the positive and negative frequency components of the Fourier spectrum. The Fourier transform of the unshifted signal  $F(\omega)$  can be expressed using the Fourier transform of the corrupted signal  $\tilde{F}(\omega)$  as

$$F(\omega) = \frac{1}{2} [\tilde{F}(\omega) + \tilde{F}^*(-\omega)] + \frac{e^{-i\omega\delta t}}{2} [\tilde{F}(\omega) - \tilde{F}^*(-\omega)]. \quad (6)$$

Taking the fast Fourier transform (FFT) of the measured signals the corrected FFTs, and consequently the corrected signals as well, can easily be calculated. This method is most effective if the number of samples in the signal processed is a power of 2.

In the time domain the data can be approximately corrected using a linear or cubic interpolation algorithm. The accuracy and speed of these correction algorithms were compared by measuring a pure sine wave from a signal generator in the  $\omega_s = [30, 50] \text{ MHz}$  frequency range with the quadrature demodulation electronics (after demodulation  $\omega = [-10, 10] \text{ MHz}$ ) and measuring the power of the corrected signal at the  $\omega' = -\omega$  ‘mirror’ frequency relative to the power at  $\omega$ . The frequency domain correction method reduces the amplitude at the mirror frequency close to the digitization level. For frequencies in the range of  $[-2, 2] \text{ MHz}$  the cubic time domain correction algorithm is comparable to the frequency domain correction. The calculation time for the time domain correction method is about 10 times shorter than for the frequency domain one, thus in most cases cubic time domain correction was applied.

After time shift correction power spectra and other quantities are calculated from the signals using standard FFT based techniques. It has to be noted that as the signals are complex, the power spectra will be asymmetric relative to 0 frequency. As in many other scattering experiments fluctuations propagating in parallel and antiparallel directions relative to the analyzing wave vector show up on the two sides of the power spectra.

As correlation analysis offers unique information from the double volume setup and the correlation of complex signals from turbulent sources is not trivial we consider this in somewhat more detail. The correlation of the complex signals in the two measurement channels can be analyzed either in the time or frequency domains. First we consider time domain correlation calculations. We wish to determine the crosscorrelation function for the two signals. These correlation functions may show time lag and correlation time of the fluctuations between the two volumes.

It has to be taken into account in the analysis that in addition to the scattering signal the measured signals contain a rather large amplitude leakage signal and a nearly white noise signal from the detectors. The leakage signal arises from light scattered out of the main beams and into the detectors from the optical components. Its frequency spectrum extends to about 50 kHz and the leakage signals in the two channels are highly correlated. This way a high-pass filtering

of the signals is essential before correlation calculation, otherwise one gets the correlation of the leakage signal. On the other hand the detector noise is uncorrelated between the two signals.

To be able to use standard correlation functions one could correlate the real or imaginary parts of the two signals. In this case one runs into interpretation problems due to the arbitrary phase between the two signals. This phase is determined by the difference in the two optical paths, and depends on wave number and volume alignment settings. To overcome this problem it was proposed in Refs. 23 and 24 to correlate the absolute squares of the complex amplitudes to obtain a correlation function that is independent of the relative phase. This correlation function was used for autocorrelation studies in Ref. 25 as well. In this case high-pass filtering for leakage signal removal before or after the amplitude calculation creates different results. If filtering is done on the raw signals, the amplitude calculation causes the detector noise to have a nonzero mean and this results in an offset in the correlation function, as was seen in Ref. 25. Additionally, scatter of the correlation function is also increased. High-pass filtering the amplitude signals avoids this problem, but causes the appearance of crossterms between the scattered signal and the leakage.

To avoid the problems described above we use the complex correlation function defined as

$$C_{12}(\tau) = \langle S_1^*(t) S_2(t + \tau) \rangle, \quad (7)$$

where subscripts 1 and 2 refer to the two measurement volumes and angular brackets denote temporal averaging. Prior to calculating the correlation function the signals are high-pass filtered to remove leakage signal. Detector noise does not appear here as distortion of the correlation values, just as a scatter on the correlation function, which can be reduced by correlating some 10 ms signals.

As the absolute magnitude of the scattering signals at different alignment of the two channels is not identical, we shall use the normalized complex correlation function

$$\bar{C}_{12}(\tau) = \frac{C_{12}(\tau)}{\sqrt{C_{11}(0)C_{22}(0)}}, \quad (8)$$

where  $C_{jj}(0)$  denotes the autocorrelation function of channel  $j$  at 0 time lag. This normalization is an approximation of the usual one where  $C_{22}$  is calculated on a time window shifted by  $\tau$  relative to the time window for the calculation of the correlation function. The present normalization where  $C_{12}$ ,  $C_{11}$ , and  $C_{22}$  are calculated in the same time windows does not guarantee that  $|\bar{C}_{12}(\tau)| \leq 1$ . However, if the time window is much longer than the maximum time lag in question and the fluctuations are stationary the above approximation is not significantly different from the usual one, but computationally more effective.

As the autocorrelation function at 0 time lag represents the total fluctuation power in the signal, it includes white noise from the detectors as well. This is indicated by a roughly  $1/f_{\max}$  wide peak in the autocorrelation function around 0 time lag as shown in Fig. 6. Here  $f_{\max}$  is the bandwidth of the detector signal determined by the digital filter-

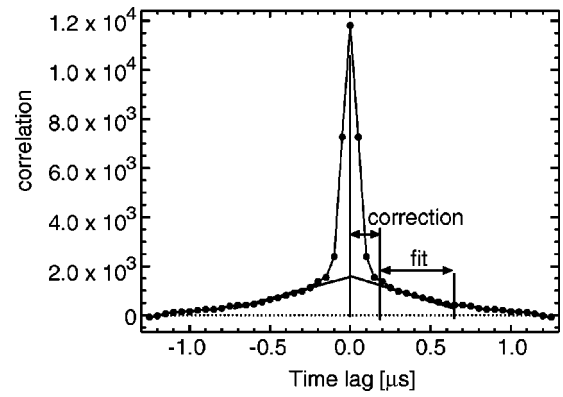


FIG. 6. Correction of autocorrelation functions used in the normalization of the correlation functions. The thin solid line with the dots is the autocorrelation function calculated from the measurement. The thick straight lines are a fit to the function in the  $[0.2, 1]$   $\mu\text{s}$  and  $[-1, -0.2]$   $\mu\text{s}$  time lag ranges. The noise peak of the autocorrelation function around 0 time lag is replaced by the fitted curve.

ing on the data acquisition card. Measurements with the present setup on W7-AS at wave numbers greater than about  $20 \text{ cm}^{-1}$  result in a detector noise amplitude comparable to the scattering signal. The normalized crosscorrelation function is therefore noticeably affected by the signal to noise ratio and its amplitude is not a faithful representation of the amplitude of the crosscorrelation function of the fluctuations in the plasma. To overcome this problem the autocorrelation functions were corrected for the noise contribution by extrapolating around 0 time lag, as explained in Fig. 6. For typical power spectra on the W7-AS stellarator this approximation proved to be adequate.

The representation of the correlation between the two signals in the frequency domain is the complex crosspower spectrum<sup>26</sup>

$$P_{12}(\omega) = F_1^*(\omega) F_2(\omega), \quad (9)$$

where  $F_j(\omega)$  is the Fourier transform of signal  $j$ . The amplitude and phase of  $P_{12}(\omega)$  are called the crosspower and crossphase, respectively. A smooth estimate for the crosspower<sup>27</sup> is obtained by averaging in frequency from the original  $\delta f = 1/T$  (where  $T$  is the sample length) resolution of the FFT transform to some  $\Delta f$  value typically in the 10–100 kHz range. For 10 ms long data samples this means averaging over  $N = \Delta f / \delta f = 100 \dots 1000$  points in the spectrum, thus the power in uncorrelated parts of the spectrum is reduced via phase mixing by factors of  $\sqrt{N} = 10 \text{--} 30$ . The remaining spectrum contains only those frequencies which are correlated in the two signals, with the power proportional to the power of the correlated fluctuations. The crosspower spectrum acts as the power spectrum of the correlated fluctuations.

The crosscorrelation function and the crosspower spectrum are two alternative representations. Depending on the phenomena either one or the other is more relevant for the analysis. To demonstrate their properties for turbulent phenomena computer generated sample signals were processed and the results are plotted in Figs. 7 and 8. As the experimentally measured power spectra shown in Sec. III B do not show any particular peaks the signals were generated from

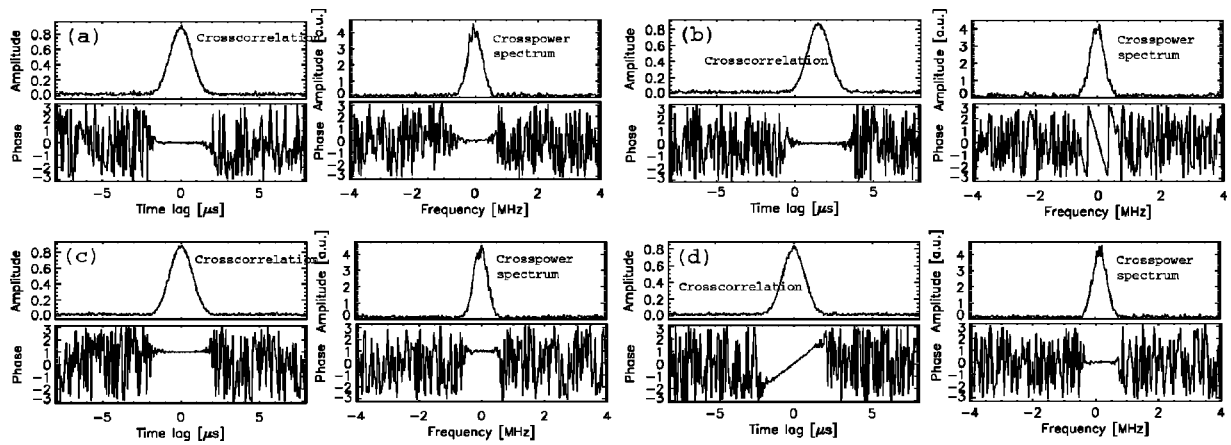


FIG. 7. Normalized correlation function and crosspower spectra of simulated signals. (a)  $\Delta_t=0, \Delta_\phi=0, v_\phi=0$ , (b)  $\Delta_t=1.5 \mu s, \Delta_\phi=0, v_\phi=0$ , (c)  $\Delta_t=0, \Delta_\phi=1, v_\phi=0$ , (d)  $\Delta_t=0, \Delta_\phi=0, v_\phi=10^6 \text{ s}^{-1}$ . See text for more explanation.

finite lifetime “events” rather than from waves. An “event” is a finite-length piece of complex signal with a Gaussian time evolution of the amplitude and a phase that is either fixed or changes linearly proportional to  $v_\phi t$ . The amplitude of these events was fixed in the simulation. The second signal was generated using the same events as for the first one but shifted in time by  $\Delta_t$  and in phase by  $\Delta_\phi$ . The signals were generated by superimposing 12 000 identical events with random phase and at random times in a  $10^6$  time unit long complex signal. The sample rate of the signals was assumed to be 20 MHz corresponding to experimental data with decimation by 4, thus the simulated signals correspond to a 50 ms measurement time. Finally, white noise was added to the two signals with an amplitude which roughly reproduces the signal/noise ratio observed in the scattering experiment. The computer simulated signals were processed with the same programs used for experimental data.

The above simulation corresponds to structures in the plasma with a fixed spatial shape whose amplitude changes as a Gaussian function in time. The amplitude and phase

measured in the two complex measurement channels represent the amplitude and phase of the structures with wave-number component at the measured  $k$ . If the phase of the signal is assumed to change linearly in time, it corresponds to a phase velocity of the fluctuations at the measured  $k$ . A time delay of  $\Delta_t$  between the two channels implies a group velocity of  $v_g=d/\Delta_t$ , where  $d$  is the separation between the two channels along the group velocity vector of the fluctuations. A fixed phase difference has no direct meaning as the relative phase of the two channels depends on the experimental setup.

Figure 7 shows normalized correlation functions and crosspower spectra of signals simulated with various parameters. For zero time delay, phase velocity, and phase delay both plots show zero phase between the two channels. It should be noted that both negative and positive frequency components are present in the crosspower plot although the fluctuations are not moving, both the phase and group velocity is 0. On plot (b) a  $1.5 \mu s$  time delay is applied between the two channels. This results in a shift of the maximum of

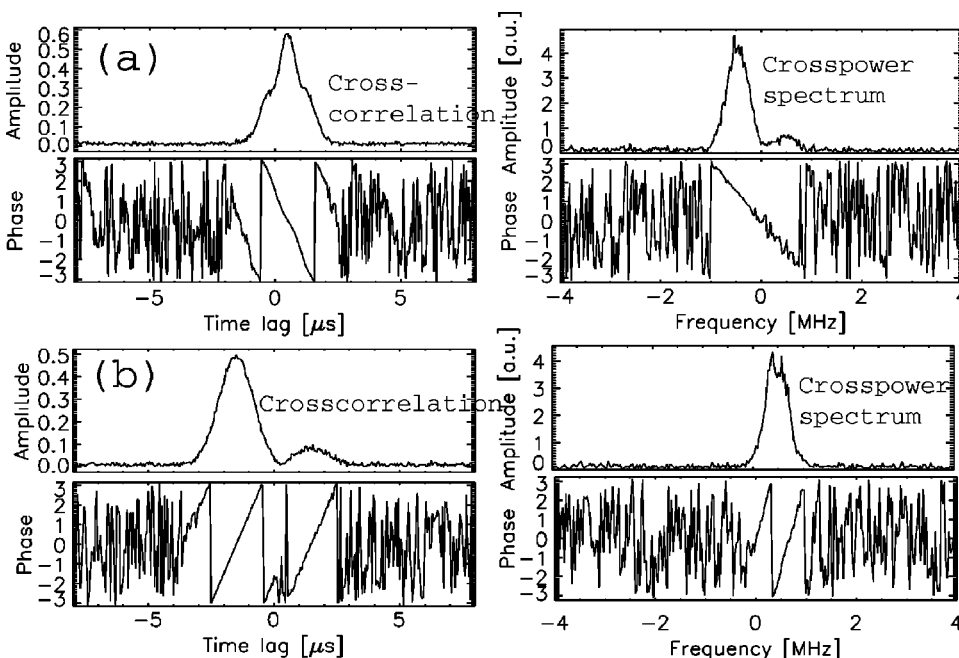


FIG. 8. Normalized correlation functions and crosspower spectra of simulated signals of two phenomena with different amplitudes: (a) Same time delay and different phase velocity; (b) different time delay and same phase velocity, see text for more explanation.

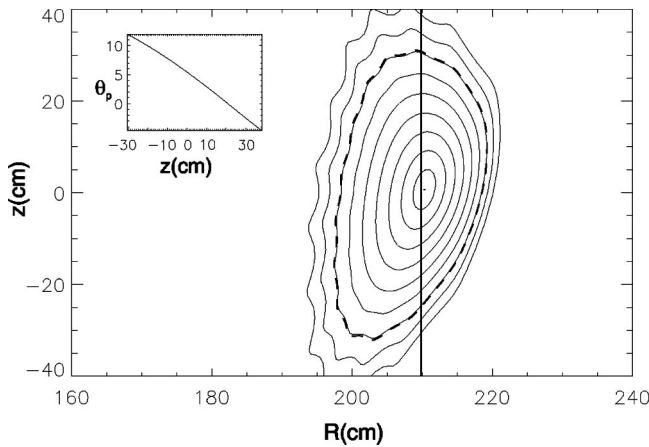


FIG. 9. Flux surface structure at the diagnostic position. The coordinate  $R$  is the major radius. The vertical line shows the center of the measurement volumes. The dashed line marks the last closed flux surface. The inset shows the magnetic field pitch angle as a function of vertical position in the plasma.

the crosscorrelation amplitude plot and a linear change in the crossphase. (Note the  $2\pi$  jumps in the phase.) The next plot (c) shows the case when a fixed phase delay is present between the channels and the phase delay clearly appears in both phase plots as a constant phase. The final plot (d) delineates correlations for the case of a nonzero phase velocity but zero group velocity. This results in a shift in the maximum of the crosspower amplitude plot and a linear phase change in the crosscorrelation phase.

If more than one phenomenon is present in the signals the crosscorrelation and crosspower spectra of the different phenomena add as complex numbers. If the phenomena are separated in phase but not in time delay [Fig. 8(a)] the crosspower spectrum is more appropriate for the separation of the two phenomena. If the frequency spectra are similar and time delays are different [Fig. 8(b)] for the phenomena the crosscorrelation function indicates the presence of more than one phenomenon better.

### III. TURBULENCE MEASUREMENTS AT W7-AS

#### A. Experimental geometry

The W7-AS experiment is a stellarator with five toroidal field periods of  $72^\circ$  each. The center of each module is at a toroidal angle  $\varphi$  of  $0^\circ$ . The  $\text{CO}_2$  laser scattering diagnostic is installed in module 4 at  $\varphi = 29.1^\circ$  where positive  $\varphi$  corresponds to the counterclockwise direction as seen from above the torus. At this position the flux surfaces are roughly elliptical having a slight tilt of the major axis relative to the vertical  $z$  axis, see Fig. 9.

The laser beams propagate vertically through the plasma as indicated by the line drawn in Fig. 9. The measurement geometry in a horizontal plane perpendicular to the direction of propagation is shown in Fig. 10. The system is most sensitive to fluctuations that propagate parallel to  $\mathbf{k}_\perp$  which can be rotated by an angle  $\alpha$  with respect to the radial coordinate  $R$  by turning the dove prism on the optical table (see Sec. II A). The “horizontal” ( $B_z$  field ignored) magnetic pitch angle shown in the figure is defined as  $\theta_p(z)$

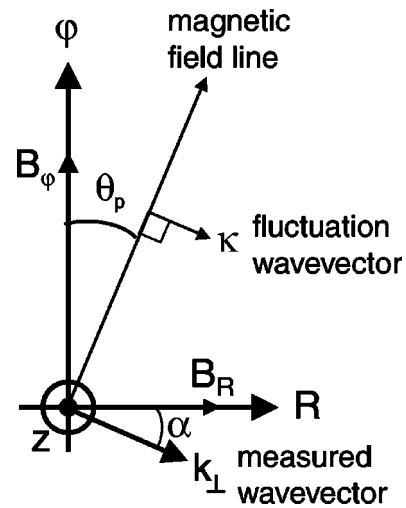


FIG. 10. Measurement geometry and magnetic field line pitch angle.

$= \text{Arctan}[B_R(z)/B_\varphi(z)]$ . With the assumption of  $\kappa_\parallel \ll \kappa_\perp$  the fluctuation wave vector  $\kappa$  is perpendicular to the field line so that the nominal angle between the fluctuations and the measured  $\mathbf{k}_\perp$  is  $\theta_p - \alpha$ . Referring to the inset in Fig. 9 we see that the pitch angle, and hence the fluctuation wave vector direction, varies approximately linearly with vertical position  $z$  ranging from  $12^\circ$  at the bottom of the plasma to  $-4^\circ$  at the top giving a total variation of  $\Delta\theta_{p,\text{tot}} = 16^\circ$ . Inside the last closed flux surface (LCFS), indicated by the dashed line in Fig. 9, the pitch angle variation is  $\Delta\theta_{p,\text{LCFS}} = 11 - (-3) = 14^\circ$ . We note that since the measurement chord passes close to the plasma center the measured  $k_\perp = k_r + k_\theta \sim k_\theta$ , where  $\theta$  is the poloidal coordinate and  $r$  is the minor radius. Thus, apart from the midplane of the torus  $z=0$ , the measured fluctuations are primarily poloidal.

#### B. Wave number spectra

As a first test of the capabilities of the instrument we present the results of a “wave number scan” experiment. A series of similar plasma discharges was produced for which  $|\mathbf{k}_\perp|$  was changed from shot to shot. The beam plane was oriented so that fluctuations perpendicular to the toroidal direction were measured ( $\alpha=0$ ). The Gaussian beam diameters ( $1/e^2$  intensity points) were 4 mm which gave measurement volumes of a length similar to the plasma diameter. The measured spectra therefore represent averages along the vertical coordinate  $z$  over the entire plasma.

The scan was performed on a series of hydrogen limiter plasmas with  $\iota_a = 0.344$  at good confinement ( $2\pi\iota_a$  is the rotational transform, i.e.,  $\iota_a$  is the number of poloidal turns per toroidal turn of the magnetic field lines at the plasma boundary). The discharges were heated by 450 kW of electron cyclotron resonance heating (ECRH) and had a toroidal magnetic field of 2.5 T. The line averaged density was kept at  $8 \times 10^{19} \text{ m}^{-3}$ . The average ion temperature was 500 eV, as determined by charge exchange measurements. This leads to a Larmor radius of 1.3 mm or converting to characteristic spatial scales  $48 \text{ cm}^{-1}$ .

The scattered power integrated over all frequencies for 150 ms (the steady-state phase) is shown in Fig. 11 and the

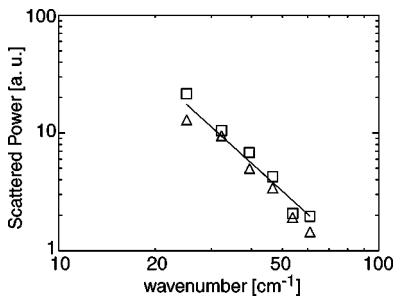


FIG. 11. Wave number scan in hydrogen plasmas. Volume 1 is marked by triangles, volume 2 by squares.

frequency dependence of the turbulence at different wave numbers is shown in Fig. 12. Small differences between the absolute turbulence levels in the two independent channels seen in Fig. 11 are due to noise and any systematic sensitivity differences between channels. The presented data have been corrected for changes in the alignment of the local oscillator beams with respect to the detectors at different wave number settings. This was done in between plasma discharges by modulating the local oscillator intensity with a fixed frequency applied to the Bragg cell and measuring the level of the detected modulation signal. Note that the data were not corrected for the change in the effective length of the measurement volume with the measured  $|\mathbf{k}_\perp|$ . Such a correction was not applied because even at the largest wave number measured the estimated measurement volume length was  $L \sim 4wk/|\mathbf{k}_\perp| \sim 0.8$  m which is larger than the height of the plasma at W7-AS. Fits to the data were calculated assuming that the fluctuation power scales as  $k_\perp^{-m}$ , with  $m$  to be determined. The estimated scaling exponent was about  $2.4 \pm 0.3$ . Numerous previous measurements of plasma turbulence in several different fusion devices have given scaling exponents in the range of about 2–4.<sup>5,15,28,29</sup>

**IV. SPATIAL LOCALIZATION**

In this section we describe spatially localized measurements using both a single wide beam (Sec. IV A) and the new two beam approach (Sec. IV B).

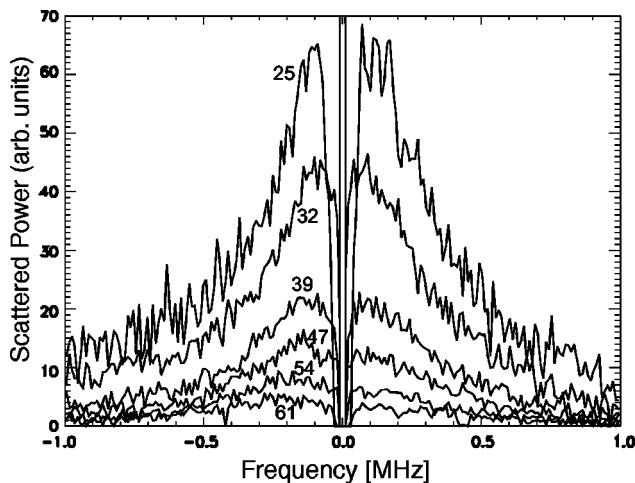


FIG. 12. Turbulence spectra at wave numbers  $\kappa = 25, 32, 39, 47, 54,$  and  $61$   $\text{cm}^{-1}$ .

**A. Single beam “magnetic” localization**

As was mentioned in Sec. II provided there are at least several fringes in the measurement volume the photodetector signal is proportional to the turbulence at wave number  $\kappa = k_\perp$ . In magnetic fusion devices the turbulence is two dimensional in a plane perpendicular to the magnetic field. Only when the measurement wave vector  $\mathbf{k}_\perp$  defined by the intersection of the main and LO beams lies in this plane will the turbulence be detected ( $\alpha = \theta_p$ ). Magnetic field pitch angle variations result in rotation of the plane of the turbulence wave vector  $\kappa$  in space. The detected signal is thus sensitive to the magnetic field pitch angle which can be used to obtain spatially localized turbulence measurements, as was first shown at Tore Supra.<sup>15</sup>

The detected heterodyne signal can be written as<sup>15</sup>

$$I(\alpha, \mathbf{k}_\perp) = \int_{L_b}^{L_t} dz \delta n^2(\mathbf{k}_\perp, z) e^{-(\alpha - \theta_p(z)/\Delta\alpha)^2}, \quad (10)$$

where  $\delta n$  is the root mean square value of the density fluctuations and the effective angular resolution is  $\Delta\alpha = \Delta\kappa/\kappa = 2/(wk_\perp) = 2/(\pi N)$ . For the measurements at W7-AS the bottom and top of the plasma were at  $L_b \sim -30$  cm and  $L_t \sim 40$  cm.

The exponential factor in Eq. (10) depends on the plasma conditions through  $\theta_p(z)$  that is determined by the externally imposed  $\theta_a$ , and the optical parameters  $\alpha, w,$  and  $k_\perp$ . When  $N$  is large the angular resolution is good and the detected signal depends sensitively on the magnetic pitch angle. In this case varying  $\alpha$  effectively selects a localized part of the measurement volume from which the detected signal originates. This method of localization is only possible under the assumption that  $\kappa_\parallel \ll \kappa_\perp$ . The validity of this assumption can be justified *a posteriori* by showing that the fluctuation “signature” changes significantly as  $\alpha$  is varied.<sup>15</sup> Stated differently, the requirement for localization is that  $\Delta\alpha \ll \Delta\theta_{p,\text{tot}}$ . This can be achieved in two ways, either by increasing  $w$  or  $k_\perp$  (or both).

We now describe the results of measurements with a single widebeam with  $w = 33$  mm. A series of six identical shots were made where we changed the horizontal direction of  $k_\perp$  from shot to shot. That is, we changed  $\alpha$  remotely between each shot. The values chosen were:  $\alpha = 12^\circ$  (bottom),  $8^\circ, 6^\circ, 4^\circ, 0^\circ,$  and  $-4^\circ$  (top). For each shot  $k_\perp$  was set to  $15 \text{ cm}^{-1}$ . The  $16^\circ$  total variation of  $\alpha$  means that the two “edge” angles give us information about the fluctuations at or beyond the LCFS. The shots were identical to the H-scan ones described in Sec. III B, except for the fact that these were D and not H plasmas.

Wide beam turbulence spectra obtained in the steady-state phase of the discharge at different vertical locations are shown in Fig. 13. Two features are apparent. First, the overall turbulence level is highest at the top and bottom of the plasma. In addition, the direction of propagation changes from top to bottom, as well as the spectral distribution of the turbulence. Separation of the direction of propagation has in the past been done using two methods: fitting the spectra to a sum of two analytical functions (Ref. 30 and references therein) or using the sign of the time derivative of the phase

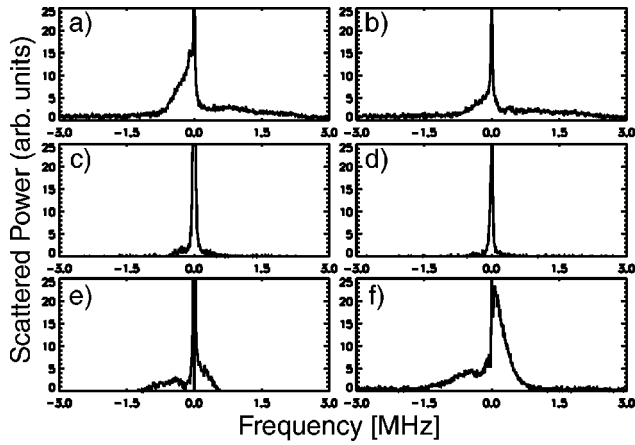


FIG. 13. Power spectra for the six different vertical measurement positions in the  $wb\ \alpha$  scan. Frames (a)–(f) show spectra from the bottom to the top of the plasma.

which reflects the direction of the fluctuations.<sup>31</sup> Insight into the temporal development of the turbulence moving in different directions can also be obtained by analyzing the time development of the turbulence in different frequency bands. This analysis is shown in Fig. 14 for positive and negative frequency bands. The D gas fueling rate serves as a confinement quality “marker.” Heavy fueling is needed in the start-up phase since this is the only particle source. As the desired constant density is reached, the fueling decreases to a constant low level. The diamagnetic energy rises steadily until about 250 ms into the discharges where it flattens, indicating a constant quality of confinement. Each of the traces shows data for all six discharges used to produce the scan. As is seen, the traces are very nearly identical meaning a good reproducibility of the plasma conditions.

As the gas fueling commences and the plasma forms the fluctuations come up and exist almost in the entire plasma cross section. After the plasma has relaxed into the steady-state phase (after 250 ms), the fluctuations have almost vanished from the central plasma column but remain visible at the edge. Remembering that Fig. 14(b) shows fluctuations with a negative frequency sign, the fluctuations at the bottom of the plasma are predominantly moving in the poloidal direction away from the torus center (see Sec. II A). On the other hand, at the top of the plasma the fluctuations are predominantly moving inwards towards the torus center, as is seen in Fig. 14(c).

The relationship of the observed direction of motion of the fluctuations to the diamagnetic drift (d.d.) directions is determined by noting that

$$\mathbf{v}_{\text{dia},q} = \frac{\mathbf{B} \times (\nabla \cdot \mathbf{P})}{nqB^2} \quad (11)$$

gives the diamagnetic drift velocity for particles of charge  $q$ , where  $n$  is the density, and  $\mathbf{P}$  is the pressure tensor. Assuming Maxwellian distributions we get  $\nabla \cdot \mathbf{P} = \nabla p$ . For these shots the density profile is rather flat and the temperature profile peaked (on-axis ECRH). Knowing that the pressure gradient is directed towards the magnetic axis and noting that the toroidal magnetic field is directed into the page in Fig. 9, we see from Fig. 14 that the dominating edge fluctuations at

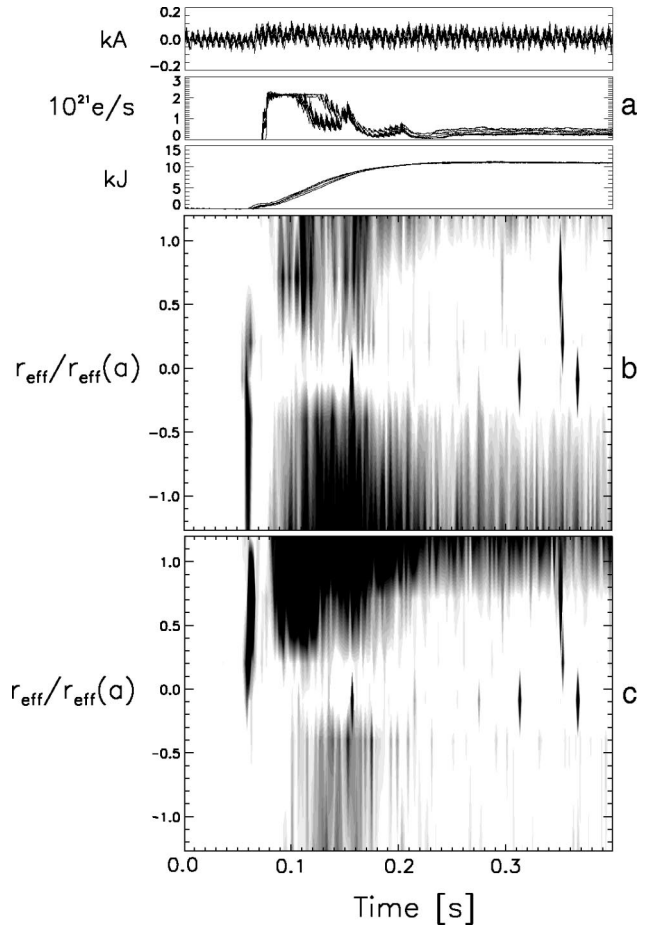


FIG. 14. Density plot of the time and vertical position resolved turbulence in two frequency bands. Frame a shows from top to bottom the plasma current, the D gas fueling rate, and the diamagnetic energy. Frame b shows the turbulence in the  $-120$  to  $-100$  kHz frequency band. Frame c shows the turbulence in the  $+100$  to  $+120$  kHz frequency band. The vertical axis corresponds to the position along the measurement volume where the detected fluctuations originate mapped into effective radius:  $r_{\text{eff}}/r_{\text{eff}}(a) = \mp 1$  correspond to the last closed flux surfaces at the bottom/top of the plasma respectively. Higher turbulence levels are shown in black.

both the top and bottom of the plasma move in the ion d.d. direction. We stress that when we discuss d.d. directions we are referring to observations in the laboratory frame  $\omega_{\text{lab}} = \omega_{\text{turb}} + \omega_{\mathbf{E} \times \mathbf{B}}$ , where  $\omega_{\text{turb}}$  is the turbulent mode frequency (e.g., drift waves) and  $\omega_{\mathbf{E} \times \mathbf{B}} = -k_{\theta} E_r / B_{\phi}$  is the Doppler shift due to the radial electric field  $E_r$ .<sup>32</sup>

In Tore Supra, the radial electric field  $E_r$  has an inversion radius of  $\rho \sim 0.95$ ,  $\rho$  being the normalized minor radius. Inside this radius  $E_r < 0$  (inward pointing), outside  $E_r > 0$  (outward pointing). Measuring fluctuations in the outer parts of the plasma one observes two peaks in the power spectrum; these are interpreted as fluctuations convected with the radial electric field. Inside/outside the inversion one observes fluctuations traveling in the electron/ion d.d. directions, respectively.<sup>30</sup> This is consistent with the sign change of  $E_r$ .

In W7-AS,  $E_r$  is derived from active charge exchange recombination spectroscopy and passive visible spectroscopy.<sup>33</sup> As is the case for Tore Supra, the electric field has an inversion radius. Within error bars it is situated at the LCFS.<sup>34</sup> Combining the fact that  $E_r$  changes sign around the LCFS and that we see large amplitude low fre-

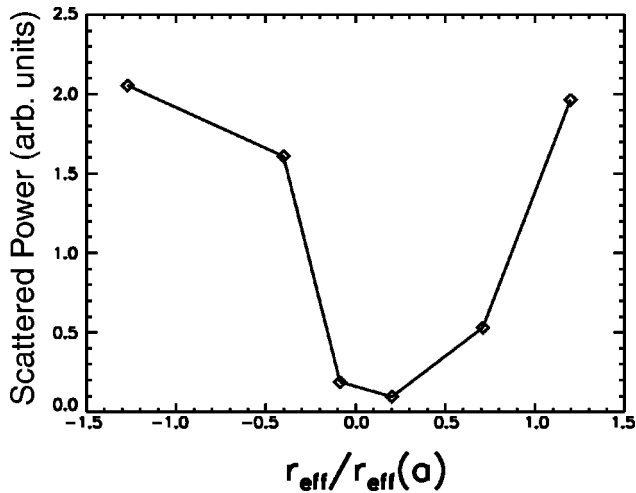


FIG. 15. Turbulence integrated over all frequencies.

quency fluctuations in the ion d.d. direction and small amplitude high frequency electron d.d. fluctuations implies that the large amplitude fluctuations are observed outside the confined plasma.

The fluctuation levels found by integrating the spectra in Fig. 13 over frequency are shown in Fig. 15 as a function of vertical position in the plasma. We see that the turbulence levels at the edge of the plasma are much higher than those in the center, as is generally observed for most toroidal fusion devices.<sup>2,4</sup> A similar picture of the spatial distribution of fluctuations was also found in recent measurements at W7-AS using a Li-beam diagnostic.<sup>20</sup> An up-down asymmetry of the size observed in Tore Supra<sup>35</sup> has not been found in W7-AS.

**B. Two beam localization**

In this section we describe the two beam approach to obtaining localized measurements based on correlation of the signals from two adjacent measurement volumes. Each measurement volume utilizes a narrow beam with a relatively small number of fringes, and the detected signal is thus insensitive to pitch angle variations along the beam. However, the signals from the two measurement volumes will only have a strong correlation when they are separated along a direction parallel to the toroidal field. In this way we recover a sensitivity to magnetic pitch angle using two narrow beams instead of a single wide beam.

Figure 16 shows the two beam geometry as seen from above. The vector  $\mathbf{d}$  determines the relative position of the two volumes;  $|\mathbf{d}|$ —the length between the centers of the volumes—is kept constant for each measurement. The angle between  $\mathbf{d}$  and the  $\varphi$  axis is denoted  $\theta_R = \text{Arcsin}(d_R/|\mathbf{d}|)$ , where  $d_R$  is the radial distance between the two volume centers. The origin of the figure (center of rotation) corresponds to the vertical line drawn at  $R = 209.8$  cm in Fig. 9. The present experimental setup allowed a maximum separation  $|\mathbf{d}|$  of 29 mm.

Let us assess the localization one can obtain with this technique. If we assume that the correlation length of the

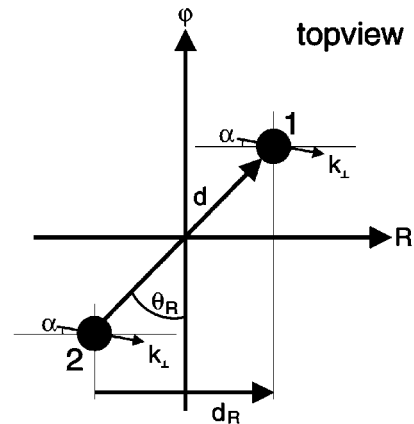


FIG. 16. Two beam measurement geometry.

fluctuations perpendicular to the magnetic field is  $L_c$  then a correlation will be seen between the two measurement signals if

$$[\theta_R - \theta_p(z)]d < L_c. \tag{12}$$

Here we assumed that the correlation length along the magnetic field lines is very much longer than the distance between the two measurement volumes, thus correlation is affected only by the  $\theta_R$  separation of the measurement volumes perpendicular to the magnetic field lines. For the given set-up  $d = 29$  mm, and in the SOL the poloidal correlation length is of order 1 cm,<sup>16</sup> thus a decorrelation of the scrape off layer (SOL) fluctuations will occur at about  $\theta_R - \theta_p \approx 20^\circ$ . As the total change of the magnetic field direction between the top and bottom LCFS is only  $14^\circ$ , the present experiment cannot be considered as a real localization, but rather as a top or bottom weighted measurement.

To show that this limited localization indeed works, experimentally measured complex correlation functions and crosspower spectra are shown in Fig. 17 at two different volume alignments. For (a) the volumes are aligned in a direction which corresponds to the magnetic field direction on top of the machine close to the LCFS, while for (b) they are aligned along the field lines at the bottom LCFS. As one can see both from the crosspower amplitude spectra and the crosscorrelation phase the fluctuations on (a) are dominated by positive phase velocities, while on (b) by negative. In both cases fluctuations with the other frequency sign are also present and their frequency spectrum extends to higher frequencies. These observations can be interpreted such that at low frequencies ( $f < 0.5$  MHz) fluctuations with positive frequencies dominate at the plasma top while negative frequencies dominate at the bottom. At higher frequencies (around 1 MHz) the tendency is reversed. This is the same conclusion reached from the wide beam localization experiment, indicating that the double beam correlation experiment is capable of providing localization along the measuring volumes.

The radial profile of the density fluctuation power can be constructed from the frequency integrated crosspower spectrum as a function of  $\Theta_R$  volume alignment. If a long enough sample length is used for the calculations the power of the uncorrelated fluctuations decreases to a low level and the

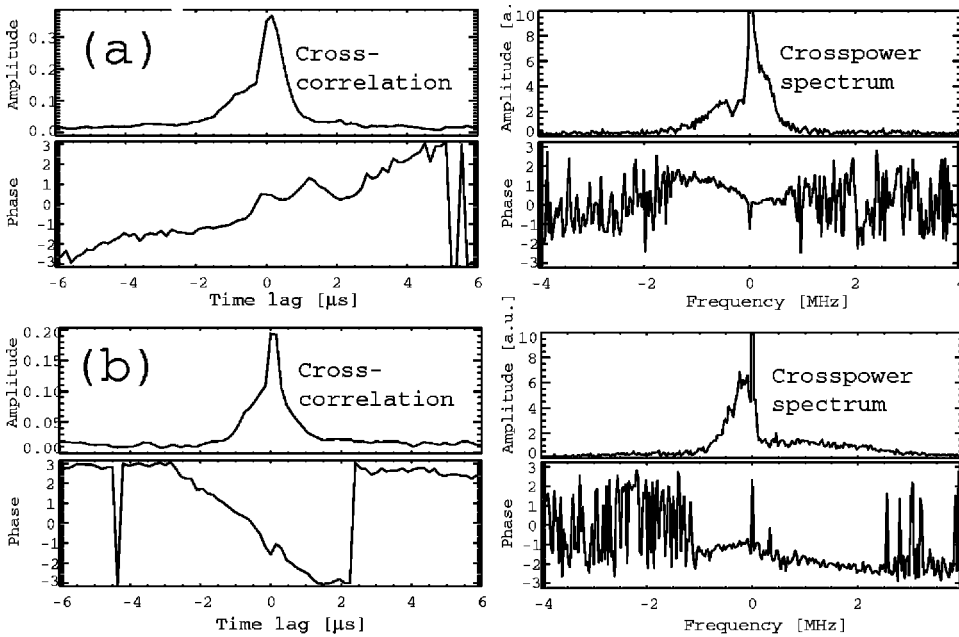


FIG. 17. Normalized correlation functions and crosspower spectra of measured signals at two different volume alignments. (a)  $-4.5^\circ$ , (b)  $+10.5^\circ$ . The measured wave number was  $\kappa = 20 \text{ cm}^{-1}$ .

turbulence aligned along  $\Theta_R$  dominates the crosspower spectrum. A fluctuation power profile calculated this way is shown in Fig. 18. The vertical bars on the plot indicate the angles of the magnetic field at the lower and upper position of the last closed flux surface. The power distribution of positive and negative low-frequency fluctuations is also plotted. The figure agrees qualitatively with the one beam localization results, the fluctuation power has a maximum close to the plasma edge and a minimum at the plasma center.

The amplitude of the crosscorrelation function deserves some attention. Using the appropriate normalization described in Sec. II D the maximum appears to be between 0.2 and 0.35. If the correlation function ideally selected fluctuations only from the top or bottom of the plasma the amplitude of the correlation function would be 0.5. As the experimentally observed correlation is more than half of this, the correlation of the fluctuations at a toroidal distance of 2.9 cm is at least 0.5.

Aligning the volumes at a larger angle the correlation disappears when the  $B_\perp$  distance of the two measurement volumes increases above approximately 1.5 cm. Figure 19 shows the frequency integrated crosspower as a function of volume alignment angle for a measurement series at  $k = 15 \text{ cm}^{-1}$ .  $\Theta_R = 10^\circ$  corresponds approximately to the plasma edge. The general trend is the same in Figs. 18 and 19, although the detailed form of the profiles are different due to different discharge conditions and measured wave numbers. The crosspower appears to drop to  $1/e$  in about  $20^\circ$ – $30^\circ$ . As the volume separation was  $d = 2.9 \text{ cm}$  this corresponds to a cross-field correlation length of about 1–1.5 cm.

V. DISCUSSION

We have described a two-volume collective scattering instrument for measurements of plasma turbulence. Data ob-

tained using a single scattering volume have been used to characterize the turbulence spectrum at W7-AS for wave numbers between 15 and  $61 \text{ cm}^{-1}$ .

A new approach to localization of the turbulence measurement along the laser path is presented which relies on the observation that the  $B_\parallel$  and  $B_\perp$  correlation lengths of plasma turbulence are expected to be very different. In agreement with expectations the correlation length in the  $B_\perp$  direction was seen to diminish at about 1.5 cm length, while along the field lines correlation extends to longer distances. With the current setup at least 0.5 correlation was seen at 3 cm toroidal distance. Using this fact a two beam measurement scheme can be built where the two measurement volumes are offset both toroidally and poloidally to achieve optimal localization.

It has to be noted that the requirement for localization

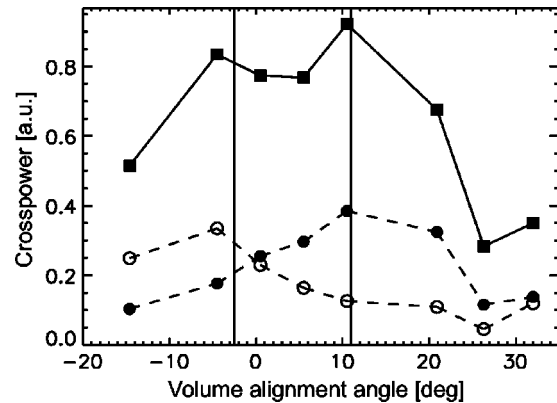


FIG. 18. Frequency integrated crosspower as a function of volume alignment angle  $\Theta_R$ . Integration frequency range  $[-1 \text{ MHz}, 1 \text{ MHz}]$ , the band  $[-50 \text{ kHz}, 50 \text{ kHz}]$  is omitted due to leakage signal. The dotted lines show the contribution of negative (closed symbols) and positive (open symbols) 0.05–0.5 MHz frequencies. The vertical bars indicate the angle of the magnetic field at the upper and lower last closed flux surfaces. Negative angles correspond to the top of the plasma. The measured wave number was  $\kappa = 20 \text{ cm}^{-1}$ .

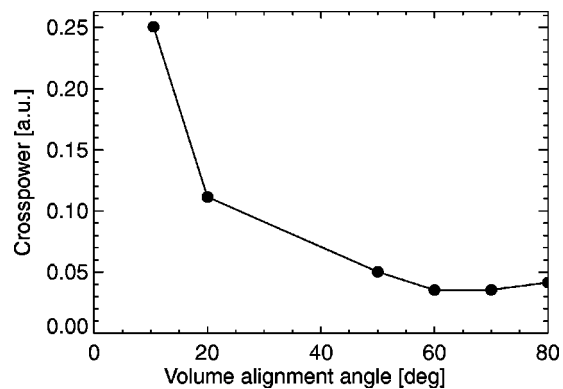


FIG. 19. Frequency integrated crosspower as a function of volume alignment angle  $\Theta_R$ . Integration frequency range  $[-1 \text{ MHz}, 1 \text{ MHz}]$ , the band  $[-50 \text{ kHz}, 50 \text{ kHz}]$  is omitted due to leakage signal. The measured wave number was  $\kappa = 15 \text{ cm}^{-1}$ .

with the double beam technique is different from the assumption  $\kappa_{\parallel} \ll \kappa_{\perp}$  that is the basis of the wide beam localization presented in Sec. IV A. For the wide beam technique localization relies on the assumption that the wave vector of the fluctuations is aligned perpendicular to the magnetic field direction. In contrast to this the double beam localization relies on assumptions about the correlation length of fluctuations. If one had long lifetime turbulent structures in the plasma, which could cover a considerable distance with the poloidal flow, the correlation criteria could be broken but the criteria on the wave vector direction could hold. Conversely, if the plasma contained structures with comparable toroidal and poloidal wave vector components that propagated along the magnetic field lines the correlation criteria might be satisfied even though the wave vector conditions were not met.

The experiments presented in this article can be considered as proof of principle results for the two beam technique where the two measuring volumes are parallel, but offset toroidally. A limited localization is clearly shown and the  $B_{\parallel}$  and  $B_{\perp}$  correlation lengths are assessed. Based on Eq. (12) one can design a double volume correlation experiment where the two volumes are displaced by a longer distance than the present 2.9 cm and additionally the two volumes can be tilted with respect to each other. In this case the straight field line approximation of Eq. (12) does not hold any more and one has to perform detailed field line tracing calculations for a given plasma configuration. An example is shown in Fig. 20. Measurement volumes are separated toroidally by 10 cm and inclined in the opposite direction by  $4^{\circ}$ . In this case correlation between the two volumes could provide a rather precise localization.

It is worth noting that this experimental arrangement can be thought of as a modified and modernized version of the crossed-beam correlation technique used in Ref. 12. In that experiment the scattering direction, and consequently the analyzing wave number, could only be set together with the position of the crossing point of the two volumes. A relatively large angle access to the plasma was also needed for the original setup. In our case the necessary angle between the two measurement volumes is provided mostly by a toroidal displacement and the more modern data acquisition can provide full temporal information on the power spectrum of

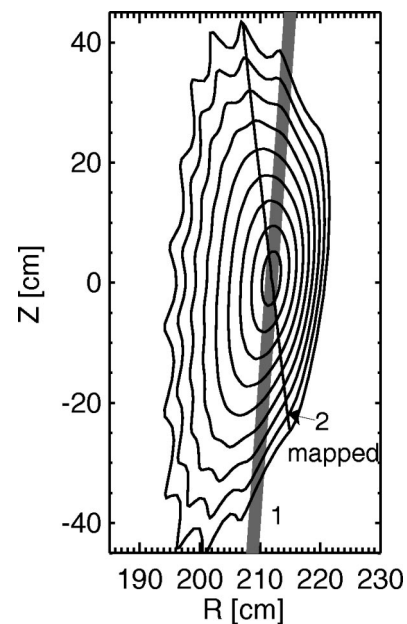


FIG. 20. A possible optimization of the experimental setup using two slightly ( $4^{\circ}$ ) inclined measurement volumes separated toroidally by 10 cm (data from W7-AS shot 47 940 at discharge time 0.3 s). The figure shows the magnetic flux surface geometry displaced 5 cm toroidally from the center of the port where measurement volume 1 is located. The shaded area represents a 2 cm wide region around measurement volume 1. The thin solid line is the mapping of measurement volume 2, located 5 cm in the other direction from the center of the port, onto the plane of volume 1.

the density fluctuations. More detailed investigations of the spatial distribution of plasma turbulence at W7-AS using the two-volume scattering instrument will be presented elsewhere.

## ACKNOWLEDGMENTS

The authors are grateful to H. Larsen for design and construction of the data acquisition card, to B. Sass and J. Thorsen for technical assistance, and to H. Niedermeyer and E. Holzhauser for helpful discussions.

- <sup>1</sup>P. C. Liewer, Nucl. Fusion **25**, 543 (1985).
- <sup>2</sup>A. J. Wootton, B. A. Carreras, H. Matsumoto, K. McGuire, W. A. Peebles, C. P. Ritz, P. W. Terry, and S. J. Zweben, Phys. Fluids B **2**, 2879 (1990).
- <sup>3</sup>U. Stroth, Plasma Phys. Controlled Fusion **40**, 9 (1998).
- <sup>4</sup>B. A. Carreras, IEEE Trans. Plasma Sci. **25**, 1281 (1997).
- <sup>5</sup>C. M. Surko and R. E. Slusher, Phys. Rev. Lett. **37**, 1747 (1976).
- <sup>6</sup>R. E. Slusher and C. M. Surko, Phys. Fluids **23**, 472 (1980).
- <sup>7</sup>E. Holzhauser, Phys. Lett. A **62**, 495 (1977).
- <sup>8</sup>E. Holzhauser and J. H. Massig, Plasma Phys. **20**, 867 (1978).
- <sup>9</sup>B. F. M. Pots, J. J. H. Coumans, and D. C. Schram, Phys. Fluids **24**, 517 (1981).
- <sup>10</sup>TFR Group, A. Truc, and D. Grésillon, Nucl. Fusion **22**, 1577 (1982).
- <sup>11</sup>H. W. H. van Andel, A. Boileau, and M. von Hellermann, Plasma Phys. Controlled Fusion **29**, 49 (1987).
- <sup>12</sup>C. M. Surko and R. E. Slusher, Phys. Fluids **23**, 2425 (1980).
- <sup>13</sup>B. A. Spivey, L. H. Sverdrup, S. H. Lin, R. G. Trissel, and W. A. Peebles, Rev. Sci. Instrum. **63**, 5252 (1992).
- <sup>14</sup>C. L. Rettig, E. J. Doyle, W. A. Peebles, K. H. Burrell, R. J. Groebner, T. H. Osborne, and N. C. Luhmann, Rev. Sci. Instrum. **66**, 848 (1995).
- <sup>15</sup>A. Truc, A. Quéméneur, P. Hennequin, D. Grésillon, F. Gervais, C. Laviron, J. Olivain, S. K. Saha, and P. Devynck, Rev. Sci. Instrum. **63**, 3716 (1992); P. Devynck, X. Garbet, C. Laviron, J. Payan, S. K. Saha, F. Gervais, P. Hennequin, A. Quéméneur, and A. Truc, Plasma Phys. Controlled Fusion **35**, 63 (1993).

- <sup>16</sup>M. Endler, L. Giannone, K. McCormick, H. Niedermeyer, A. Rudyi, G. Theimer, N. Tsois, and S. Zoletnik, *Phys. Scr.* **51**, 610 (1995).
- <sup>17</sup>R. J. Fonck, G. Cosby, R. D. Durst, S. F. Paul, N. Bretz, S. Scott, E. Synakowski, and G. Taylor, *Phys. Rev. Lett.* **70**, 3736 (1993).
- <sup>18</sup>Type PCI-L-3 from Vigo Systems Ltd. Commercial model name used here for technical communication only.
- <sup>19</sup>See, for example, I. H. Hutchinson, *Principles of Plasma Diagnostics* (Cambridge University Press, Cambridge, 1987).
- <sup>20</sup>S. Zoletnik, M. Anton, M. Endler, S. Fiedler, M. Hirsch, K. McCormick, J. Schweinzer, and the W7-AS team, *Phys. Plasmas* **6**, 4239 (1999).
- <sup>21</sup>E. L. Dereniak and G. D. Boreman, *Infrared Detectors and Systems* (Wiley, New York, 1996).
- <sup>22</sup>The value of  $G$  used in the text is taken from the manufacturers data for the maximum bias current of 10 mA. In practice it was found that parasitic frequency spikes could appear at maximum bias current and the detectors were typically operated at a lower bias, and hence a lower gain. The actual detector sensitivity may therefore be lower than the estimate given here.
- <sup>23</sup>L. Lading, M. Saffman, S. G. Hanson, and R. V. Edwards, *J. Atmos. Terr. Phys.* **58**, 1013 (1996).
- <sup>24</sup>N. P. Heinemeier, RISØ Laboratory Report Risø-R-1064(EN) 1998.
- <sup>25</sup>G. Antar, F. Gervais, P. Hennequin, A. Quéméneur, R. Sabot, A. Truc, P. Devynck, C. Fenzi, X. Garbet, and C. Laviron, *Plasma Phys. Controlled Fusion* **40**, 947 (1998).
- <sup>26</sup>E. J. Powers, *Nucl. Fusion* **14**, 749 (1974).
- <sup>27</sup>J. S. Bendat and A. G. Piersol, *Random Data: Analysis and Measurement Procedures* (Wiley, New York, 2000).
- <sup>28</sup>S. F. Paul, N. Bretz, R. D. Durst, R. J. Fonck, Y. J. Kim, E. Mazzucato, and R. Nazikian, *Phys. Fluids B* **4**, 2922 (1992).
- <sup>29</sup>G. J. J. Remkes, A. J. H. Donne, H. DeKluiver, and F. C. Schuller, *Plasma Phys. Controlled Fusion* **34**, 1379 (1992).
- <sup>30</sup>D. Grésillon, B. Cabrit, J. P. Villain, C. Hanuise, A. Truc, C. Laviron, P. Hennequin, F. Gervais, A. Quemeneur, X. Garbet, J. Payan, and P. Devynck, *Plasma Phys. Controlled Fusion* **34**, 1985 (1992).
- <sup>31</sup>G. Antar, P. Devynck, C. Laviron, P. Hennequin, X. Garbet, A. Truc, R. Sabot, A. Quéméneur, C. Honoré, C. Fenzi, and F. Gervais, *Plasma Phys. Controlled Fusion* **41**, 733 (1999).
- <sup>32</sup>R. Philipona, E. J. Doyle, N. C. Luhmann, W. A. Peebles, C. L. Rettig, R. J. Groebner, K. H. Burrell, P. Gohil, H. Matsumoto, and R. D. Stambaugh, *Phys. Fluids B* **5**, 87 (1993).
- <sup>33</sup>J. Baldzuhn, M. Kick, H. Maassberg, and the W7-AS Team, *Plasma Phys. Controlled Fusion* **40**, 967 (1998).
- <sup>34</sup>J. Baldzuhn (private communication, 1999).
- <sup>35</sup>C. Fenzi, P. Devynck, A. Truc, X. Garbet, H. Capes, C. Laviron, G. Antar, F. Gervais, P. Hennequin, and A. Quéméneur, *Plasma Phys. Controlled Fusion* **41**, 1043 (1999).